Balzani, V.; Clemente-Leon, M.; Credi, A.; Ferrer Ribera, RB.; Venturi, M.; Flood, A.; Stoddart, J. (2006). Autonomous artificial nanomotor powered by sunlight. Proceedings of the National Academy of Sciences. 103(5):1178-1183. doi:10.1073/pnas.0509011103.

PHYSICAL SCIENCES

An Autonomous Artificial Nanomotor Powered by Sunlight

Vincenzo Balzani*[†], Miguel Clemente-León[*‡], Alberto Credi[*†], Belén Ferrer[*§], Margherita Venturi[*], Amar H. Flood[¶], J. Fraser Stoddart[¶†]

[*]Dipartimento di Chimica "G. Ciamician", Università di Bologna, via Selmi 2, 40126 Bologna, Italy; [¶]The California NanoSystems Institute and the Department of Chemistry and Biochemistry, University of California, Los Angeles, 405 Hilgard Avenue, Los Angeles, California 90095-1569, USA.

REVISED VERSION

[†]To whom correspondence should be addressed. E-mail: vincenzo.balzani@unibo.it, Phone: +39 051 2099560, Fax: +39 051 2099456; E-mail: alberto.credi@unibo.it, Phone: +39 051 2099540, Fax: +39 051 2099456; E-mail: stoddart@chem.ucla.edu, Phone: +1 310 206 7078, Fax: +1 310 206 1843.

[‡]Present address: Instituto de Ciencia Molecular, Universidad de Valencia, Dr. Moliner 20, 46100 Burjassot, Spain

[§]Present address: Departamento de Química, Universidad Politécnica de Valencia, Camino de Vera s/n, 46022 Valencia, Spain

ABSTRACT

Light excitation powers the reversible shuttling movement of the ring component of a rotaxane between two stations located at a 1.3 nm distance on its dumbbell-shaped component. The photoinduced shuttling movement, which occurs in solution, is based on a "four stroke" synchronized sequence of electronic and nuclear processes. At room temperature the deactivation time of the high-energy charge-transfer state obtained by light excitation is about 10 μs, and the time period required for the ring displacement process is on the order of 100 μs. The rotaxane behaves as an autonomous linear motor and operates with a quantum efficiency up to ~12%. The investigated system is a unique example of an artificial linear nanomotor because it gathers together the following features: (i) it is powered by visible light (e. g., sunlight); (ii) it exhibits autonomous behavior, like motor proteins; (iii) it does not generate waste products; (iv) its operation can rely only on intramolecular processes, allowing in principle operation at the single-molecule level; (v) it can be driven at a frequency of 1 kHz; (vi) it works in mild environmental conditions (i. e., fluid solution at ambient temperature); and (vii) it is stable for at least 10^3 cycles.

INTRODUCTION

The miniaturization race is encouraging scientists to design and construct motors on the nanometer scale, that is, at the molecular level (1,2,3,4,5). Such a daring goal finds its scientific origin in the existence of natural molecular motors (6,7,8,9).

Natural molecular motors, however, are extremely complex, and any attempt to construct systems of such a complexity, using the bottom-up molecular approach (10,11), would be challenging. What can be done, at present, is to construct simple prototypes of artificial

molecular motors and machines (1,2,3,4,5,12,13,14,15,16,17,18,19,20,21,22,23,24,25,26), consisting of a few components capable of moving in a controllable way, and to investigate the associated problems posed by interfacing them with the macroscopic world (27,28,29,30,31,32,33), particularly as far as energy supply is concerned.

Natural motors are *autonomous*: they keep operating, in a constant environment, as long as the energy source is available. By contrast, apart from a few recent examples (34,35,36), the fuel-powered artificial motors described so far are *not autonomous* since, after the mechanical movement induced by a chemical input, they need another, opposite chemical input to reset, which also implies generation of waste products. Addition of a fuel, however, is not the only means by which energy can be supplied to a chemical system. In fact, Nature shows that, in green plants, the energy needed to sustain the machinery of life is ultimately provided by sunlight. Energy inputs in the form of photons can indeed cause mechanical movements by reversible chemical reactions without formation of waste products (15,16,17,20,21).

In a previous paper (37) we reported on the rotaxane $\mathbf{1}^{6+}$ (Scheme 1) that was carefully designed and synthesized to perform as a linear molecular motor powered exclusively by visible light, with autonomous operation relying on intramolecular processes. In such a paper, however, we only succeeded to demonstrate the operation of the rotaxane as a light driven mechanical switch that needed alternate addition of two "fuels", namely triethanolamine and oxygen, with concomitant generation of waste products. In this article we are able to show that $\mathbf{1}^{6+}$ does behave as an autonomous "four stroke" motor powered only by sunlight, without generation of waste products. We have measured the rate constants and the efficiences of the electronic and nuclear processes on which the shuttling movement is based, and we have also discussed the related energetic aspects.

Just like their macroscopic counterparts, molecular-level machines have to be organized structurally and work as functionally integrated multicomponent systems (1). The rotaxane $\mathbf{1}^{6+}$ consists of as many as six molecular components suitably chosen and assembled in order to achieve the devised function. It comprises a bis-*p*-phenylene-34-crown-10 electron donor macrocycle **R** (hereafter called the ring), and a dumbbell-shaped component which contains two electron acceptor recognition sites for the ring, namely a 4,4′-bipyridinium ($\mathbf{A_1}^{2+}$) and a 3,3′-dimethyl-4,4′-bipyridinium ($\mathbf{A_2}^{2+}$) units, that can play the role of "stations" for the ring **R**. Molecular modelling shows that the overall length of $\mathbf{1}^{6+}$ is about 5 nm and the distance between the centers of the two stations, measured along the dumbbell, is about 1.3 nm. Furthermore, the dumbbell-shaped component incorporates a $[Ru(bpy)_3]^{2+}$-type (bpy = 2,2′-bipyridine) electron transfer photosensitizer $\mathbf{P}^{2+}$ which is able to operate with visible light and also plays the role of a stopper, a *p*-terphenyl-type rigid spacer **S** which has the task of keeping the photosensitizer far from the electron acceptor units, and finally a tetraarylmethane group **T** as the second stopper, crucial for the template-directed slippage synthesis of the rotaxane $\mathbf{1}^{6+}$ from the ring **R** and its dumbbell-shaped precursor $\mathbf{2}^{6+}$.

RESULTS AND DISCUSSION

Electrochemical Switching

Electrochemical and nuclear magnetic resonance (NMR) spectroscopic data showed (37) that the stable conformation of $\mathbf{1}^{6+}$ is by far the one in which the **R** component is located around the better electron acceptor station, $\mathbf{A_1}^{2+}$, as represented in Scheme 1. When the interaction between **R** and $\mathbf{A_1}^{2+}$ is switched off by selective reduction of $\mathbf{A_1}^{2+}$ to $\mathbf{A_1}^{+}$ (–0.44 V versus saturated calomel electrode, SCE), the ring **R** moves by Brownian motion (9,25) to the alternative $\mathbf{A_2}^{2+}$

station. Successive oxidation restores the electron acceptor power of the $\mathbf{A_1}^{2+}$ station and therefore the ring **R** moves back again by Brownian motion to surround this station.

We have carried out in acetonitrile solution spectroelectrochemical experiments by exhaustive one-electron reduction of $\mathbf{1}^{6+}$ and $\mathbf{2}^{6+}$ at a potential of –0.50 V versus SCE. The spectra so obtained (Figure 1) display the characteristic absorption bands (38), at around 390 and 600 nm, of the one-electron reduced form of 4,4′-bipyridinium ($\mathbf{A_1}^{+}$) moiety. There is no evidence for the formation of the one-electron reduced form of 3,3′-dimethyl-4,4′-bipyridinium ($\mathbf{A_2}^{+}$), which has a substantially different absorption spectrum (39).

Photochemical Switching

The $[Ru(bpy)_3]^{2+}$-type unit $\mathbf{P}^{2+}$ (Scheme 1) is capable of playing the role of a photosensitizer for ring shuttling since visible light excitation leads to the formation of a long lived strongly reducing excited state. Except for luminescence quantum yield and lifetime (vide infra), the photophysical and electrochemical properties of the photosensitizer $\mathbf{P}^{2+}$ unit contained in $\mathbf{1}^{6+}$ and $\mathbf{2}^{6+}$ are the same as those exhibited by the model compound $\mathbf{3}^{2+}$ – absorption: λ_{max} = 458 nm, ε_{max} = 14800 L mol^{-1} cm^{-1}; emission: λ_{max} = 618 nm, τ = 880 ns; Φ_{em} = 0.065; excited state energy ca. 2.1 eV; $E_{1/2}(\mathbf{P}^{2+}/\mathbf{P}^{+})$ = +1.15 V versus SCE. It is worthwhile recalling that the $\mathbf{P}^{2+}$ unit can harvest sunlight quite efficiently because it displays a broad and intense absorption band in the visible region.

The overall mechanism devised to perform the light-driven shuttling process in the rotaxane $\mathbf{1}^{6+}$ is based on the following four phases (Scheme 2a):

(a) *Destabilization of the stable conformation*: light excitation of the photoactive unit $\mathbf{P}^{2+}$ (step 1) is followed by the transfer of an electron from the $*\mathbf{P}^{2+}$ excited state to the $\mathbf{A_1}^{2+}$ station,

which is encircled by the ring **R** (step 2), with the consequent "deactivation" of this station; such a photoinduced electron-transfer process has to compete with the intrinsic decay of $*\mathbf{P}^{2+}$ (step 3).

(b) *Ring displacement*: after reduction ("deactivation") of the $\mathbf{A_1}^{2+}$ station to $\mathbf{A_1}^{+}$, the ring moves by Brownian motion to $\mathbf{A_2}^{2+}$ (step 4), a step that has to compete with back electron-transfer from $\mathbf{A_1}^{+}$ to the oxidized photoactive unit $\mathbf{P}^{3+}$ (step 5). This requirement is the most difficult one to meet since step 4 involves only slightly exergonic nuclear motions whereas step 5 is an exergonic outer-sphere electron transfer process.

(c) *Electronic reset*: a back electron-transfer process from the "free" reduced station $\mathbf{A_1}^{+}$ to $\mathbf{P}^{3+}$ (step 6) restores the electron acceptor power of the $\mathbf{A_1}^{2+}$ station.

(d) *Nuclear reset*: as a consequence of the electronic reset, the ring moves back again by Brownian motion from $\mathbf{A_2}^{2+}$ to $\mathbf{A_1}^{2+}$ (step 7).

In order to verify whether such a devised mechanism works, we have performed luminescence quenching and flash photolysis experiments both in the absence and presence of phenothiazine as an electron relay.

Luminescence quenching. In deaerated acetonitrile solution containing the rotaxane $\mathbf{1}^{6+}$ or the dumbbell-shaped compound $\mathbf{2}^{6+}$, the emission lifetimes and intensities of the $\mathbf{P}^{2+}$ units are quenched when compared with the values obtained for the model compound $\mathbf{3}^{2+}$. The luminescence lifetime values at different temperatures for rotaxane $\mathbf{1}^{6+}$, dumbbell-shaped component $\mathbf{2}^{6+}$ and reference compound $\mathbf{3}^{2+}$ are reported in Table 1. The occurrence of dynamic quenching can be ruled out because of the high dilution of the solution. As it will be clear from the transient absorption data, the luminescence quenching is due to an electron transfer process from the $*\mathbf{P}^{2+}$ excited state to the $\mathbf{A_1}^{2+}$ unit. The electron transfer rate constant k_{et} (step 2, Scheme 2a) can be obtained from equation 1:

$$k_{et} = \frac{1}{\tau} - k_d \qquad (1)$$

where τ is the luminescence lifetime and k_d, the rate constant for the deactivation of $^*\mathbf{P}^{2+}$ by all pathways other than electron transfer (step 3, Scheme 2a), is given by $1/\tau_0$, where τ_0 is the luminescence lifetime of the reference compound $\mathbf{3}^{2+}$. The quantum yield values for the electron transfer process can be obtained from equation 2:

$$\Phi_{et} = \frac{k_{et}}{k_{et} + k_d} = k_{et} \times \tau \qquad (2)$$

The results obtained are gathered in Table 1.

Flash photolysis. Upon flash excitation of $\mathbf{1}^{6+}$, transient absorption spectral changes were observed (Figure S1, Supporting Information). The transient spectrum 6 μs after light excitation displayed the features of the monoreduced 4,4′-bipyridinium unit $\mathbf{A_1}^+$ (for the monoreduced form of the 1,1′-dibenzyl-4,4′-bipyridinium model compound in acetonitrile, λ_{max} = 402 nm and ε_{max} = 35000 M^{-1} cm^{-1}), and some residual bleaching in the spectral region of the ground state absorption of $\mathbf{P}^{2+}$. There is no evidence of formation of the monoreduced 3,3′-dimethyl-4,4′-bipyridinium unit, $\mathbf{A_2}^+$, whose spectrum (39) is substantially different from that of $\mathbf{A_1}^+$. These results indicate that the species formed upon light excitation of $\mathbf{1}^{6+}$ is a compound in which an electron has been transferred from the $^*\mathbf{P}^{2+}$ excited state to the $\mathbf{A_1}^{2+}$ unit. The same results have been obtained for dumbbell $\mathbf{2}^{6+}$.

In the case of model compound $\mathbf{3}^{2+}$, where photoinduced electron transfer cannot take place because it does not contain any electron acceptor unit, the observed spectral changes were consistent with the formation of the excited state of the $\mathbf{P}^{2+}$ unit (Figure S2, Supporting

Information). The decay time of the transient absorption spectrum was in full agreement with the luminescence decay. An isosbestic point between the absorption spectra of the ground and excited states of the $\mathbf{P}^{2+}$ unit in such a model compound was found at λ_{iso}= 398 nm. This observation and the fact that the spectrum of $\mathbf{A_1}^{+}$ possesses (38) a very intense band peaking in the same region (Figure 1) allowed us to monitor the formation and decay of the $\mathbf{A_1}^{+}$ unit in the case of $\mathbf{1}^{6+}$ and $\mathbf{2}^{6+}$, and hence to measure the rate constants for the forward ($^*\mathbf{P}^{2+}$ to $\mathbf{A_1}^{2+}$, step 2, Scheme 2a) and the back ($\mathbf{A_1}^{+}$ to $\mathbf{P}^{3+}$, steps 5 and 6, vide infra) electron transfer processes. Typical transient absorption kinetics recorded at λ_{iso} are shown in Figure 2.

The changes of the transient absorption, monitored at λ_{iso}, as a function of time were measured at five different temperatures (the exact position of λ_{iso} was determined on model compound $\mathbf{3}^{2+}$ at each temperature). In all cases, the rise time of the transient absorption was in agreement, within experimental error (20%), with the lifetime of the excited state of the $\mathbf{P}^{2+}$ component (Table 1), and the transient absorption signal completely disappeared with the first-order rate constants, k_{bet} reported in Table 2. We have also observed that both $\mathbf{1}^{6+}$ and $\mathbf{2}^{6+}$ do not undergo any photodegradation after 10^3 light pulses. The quantum yields of the photoinduced electron transfer processes obtained from transient absorption data (Supporting Information) are in agreement, within experimental error, with those found from luminescence measurements.

In summary, the luminescence and transient absorption data demonstrate that visible excitation of the $\mathbf{P}^{2+}$ component in $\mathbf{1}^{6+}$ and $\mathbf{2}^{6+}$ causes an electron transfer process (k_{et}) to the $\mathbf{A_1}^{2+}$ unit, followed by a back electron transfer (k_{bet}) leading to the ground state according to a monoexponential law (Table 2).

In the rotaxane $\mathbf{1}^{6+}$ the back electron transfer can take place by either step 5 or 6 (Scheme 2a), depending on the rate of ring displacement (step 4). If step 5 is much faster than step 4, the photoinduced electron transfer is simply followed by a back electron transfer, without any ring

motion. If, on the contrary, step 4 is much faster than step 5, the photoinduced electron transfer causes the displacement of the ring **R** from the $\mathbf{A_1}^+$ station to $\mathbf{A_2}^{2+}$. In such a case, back electron transfer (now, step 6) leads subsequently to the unstable isomer of $\mathbf{1}^{6+}$ (D in Scheme 2a) which relaxes thermally (step 7) to give back the starting conformation. If the rates of steps 4 and 5 are not much different from each other, both steps 5 and 6 contribute to the back electron transfer process. The above discussed results showed that steps 1, 2, 3, and 5 and/or 6 take place, but we were not able to establish whether the photoinduced ring displacement, step 4, occurs (Scheme 2a). This problem has been tackled as discussed below.

Experiments in the presence of phenothiazine as an electron relay. We have employed an electron relay to slow down the back electron transfer process (step 5) so as to observe the ring displacement (step 4) and measure its rate.

A compound **X** capable of playing the role of an electron relay in our system must satisfy several requirements: (i) it should not quench the $\mathbf{*P}^{2+}$ excited state by energy transfer, (ii) its oxidation process must be chemically reversible, (ii) its $\mathbf{X}^+/\mathbf{X}$ redox potential must be less positive than that of $\mathbf{P}^{3+}/\mathbf{P}^{2+}$ (+1.15 V versus SCE) in order to scavenge $\mathbf{P}^{3+}$, and (iv) both **X** and $\mathbf{X}^+$ should not absorb the light used to cause the photoreaction and to monitor its occurrence. After having tried and discarded several compounds (DABCO, diphenylamine and triphenylamine), we have chosen phenothiazine, **ptz,** which is reversibly oxidized [$E_{½}(\mathbf{ptz}^+/\mathbf{ptz})$ = +0.60 V versus SCE] (40) and does not show absorption bands in the visible region. Furthermore its radical cation $\mathbf{ptz}^+$ exhibits a band around 520 nm (41) that does not interfere with the spectrum of $\mathbf{A_1}^+$ and can also be useful for monitoring the behavior of the electron relay during the process.

When photoexcitation of $\mathbf{1}^{6+}$ is performed in the presence of **ptz** (Scheme 2b), the photoinduced electron transfer (step 2) is expected to be followed by a diffusion controlled reaction between **ptz** and $\mathbf{P}^{3+}$ with formation of $\mathbf{ptz}^{+}$ and regeneration of $\mathbf{P}^{2+}$ (step 8). Therefore, *intramolecular* back electron transfer (step 5) should no longer occur and ring displacement (step 4) should successfully compete with the much slower *intermolecular* back electron transfer reaction between $\mathbf{ptz}^{+}$ and $\mathbf{A_1}^{+}$ (step 9).

Flash photolysis experiments of solutions containing $\mathbf{1}^{6+}$ or $\mathbf{2}^{6+}$ (1.0×10^{-4} mol L^{-1}) and phenothiazine (5.0×10^{-5} mol L^{-1}) at all the examined temperatures showed the presence of the characteristic bands of $\mathbf{A_1}^{+}$ around 390 and 600 nm, and of $\mathbf{ptz}^{+}$ around 520 nm (Figure 3). The transient absorption signals at 600, 520 and 390 nm completely disappeared according to identical second order processes occurring in the millisecond time-scale (Table 2 and Figure 3, inset). Therefore under such conditions the back electron transfer reaction is much slower (from two to three orders of magnitude) than in the absence of **ptz,** thereby leaving more time for ring displacement.

In order to measure the rate of ring displacement we have carefully analyzed the time evolution of the shape of the 390 nm transient absorption band of the reduced station $\mathbf{A_1}^{+}$ (see Supporting Information). We have found that the maximum of such a band in $\mathbf{1}^{5+}$ undergoes a slight red shift upon decay, whereas it does not change for $\mathbf{2}^{5+}$ (Figure 4a) that has the same structural elements of the rotaxane – except for the "movable" ring – and features all the processes which allow the operation of the motor but the motion of the ring itself. The shift of the maximum of the $\mathbf{A_1}^{+}$ band in $\mathbf{1}^{5+}$ that accompanies the transient signal decay can thus be related to the displacement of the ring from $\mathbf{A_1}^{+}$ to $\mathbf{A_2}^{2+}$ ($k_{rd,}$ step 4 in Scheme 2a). This assumption is supported by the fact that, 850 μs after light excitation (303 K), the transient UV band in the case of $\mathbf{1}^{6+}$ is slightly red shifted compared to that observed for $\mathbf{2}^{6+}$ (Figure 4a) as

observed in the spectroelectrochemical experiments between the one electron reduced form $\mathbf{1}^{5+}$ (in which the ring encircles $\mathbf{A_2}^{2+}$) and $\mathbf{2}^{5+}$ (Figure 1).

A kinetic analysis (see ref. 16 and Supporting Information) has shown that the shift of the band maximum (i. e., the ring displacement) takes place according to a monoexponential law (Figure 4a) with a rate constant, k_{rd}, that rises with increasing temperature (Table 2, Figure 4b). The free energy of activation for the ring displacement is about 50 kJ mol^{-1} at 298 K. The relatively small values of the ring displacement rate constants suggest that such a movement requires considerable structural rearrangements, possibly including unfolding processes (42). Under the experimental conditions used both $\mathbf{1}^{6+}$ or $\mathbf{2}^{6+}$ showed a reversible behavior, with no change in the steady-state absorption and luminescence spectra after 10^3 laser pulses.

In conclusion, in the presence of **ptz** the photoinduced electron transfer reaction (step 2) is unaffected (for more details see Supporting Information), $\mathbf{P}^{3+}$ is completely scavenged by **ptz** (step 8), ring displacement takes place (step 4), and both electron (steps 9 and/or 10) and nuclear (step 7) reset processes occur quantitatively since the system can undergo at least 10^3 cycles. Therefore $\mathbf{1}^{6+}$ behaves as an autonomous molecular motor which consumes *only* photons of visible light (Scheme 2b). The role played by **ptz** is that of an electron relay with a "negative" kinetic effect.

Intramolecular mechanism. As reported above, by using **ptz** as an electron relay we have obtained the rate (k_{rd}, Table 2) of ring displacement (step 4) from the photogenerated $\mathbf{A_1}^{+}$ station to the $\mathbf{A_2}^{2+}$ station. Therefore we can go back to the discussion about what happens in the absence of **ptz** (Scheme 2a). In order to understand whether ring displacement takes place also in the case of the intramolecular mechanism, we must compare the values of k_4 (i. e., k_{rd}) and k_5, the rate of the back electron-transfer process from the $\mathbf{A_1}^{+}$ station, still encircled by the ring, to $\mathbf{P}^{3+}$.

The kinetic treatment and more details are given in Supporting Information. Contrary to what happens when **ptz** is present, in the case of the intramolecular mechanism the exact position of $\mathbf{A_1}^+$ absorption maximum and, if any, its shift during the signal decay cannot be established because of interference by the absorption spectra of $^*\mathbf{P}^{2+}$ and $\mathbf{P}^{3+}$. However, we can estimate the rate constant of step 6 from the experiments performed on the dumbbell component $\mathbf{2}^{6+}$ ($k_{bet} = k_6$) and we can reasonably assume that k_{rd} is the same as that observed for the **ptz**-assisted mechanism. From Table 2 we can see that k_6 (i. e., k_{bet} for $\mathbf{2}^{6+}$) is at least 35 times larger than k_{rd}, so that conformer C has to disappear (step 6) as soon as it is formed (step 4). Therefore in $\mathbf{1}^{6+}$ $k_{bet} = k_5 + k_{rd}$. At 303 K (Table 2) $k_5 = 1.5\times10^5 - 2.1\times10^4 = 1.3\times10^5$ s^{-1}, which means that the displacement of the ring (step 4) competes (14%) with the intramolecular back electron transfer (step 5, Scheme 2a). In conclusion, *also in the absence of **ptz**, the shuttling process does take place with appreciable efficiency* at 303 K. The drawback of the low efficiency (for more details, see next section) is compensated by the fact that the operation of the system relies *exclusively* on intramolecular processes. This artificial molecular motor does not rely on consumption or even assistance of external species, it is stable for at least 10^3 cycles and it operates by simply exposing the solution to sunlight.

Shuttling Efficiency

As we have seen above, the results obtained have allowed us to establish the following relationship among the rate constants of the steps involved in the intramolecular and **ptz**-assisted mechanisms (Scheme 2) and the experimentally determined rate constants (Tables 1 - 3): $k_2 = k_{et}$ (Table 2); $k_3 = 1/\tau_0$ (Table 1); $k_4 = k_{rd}$ (Table 2); $k_5 = k_{bet} - k_{rd}$ (Table 3); k_6 and k_{10} are obtained from the experimentally measured k_{bet} of $\mathbf{2}^{6+}$ (Table 2); k_9 is obtained from equation S11 (Table 3, in which the values of $k_9[\mathbf{ptz}^+]_0$, more easily comparable with k_4, are reported). Concerning

step 8, its rate constant is diffusion controlled, $k_8 \approx 1\times10^{10}$ L mol^{-1} s^{-1}, and under our experimental conditions it is fast enought to fully prevent intramolecular back electron transfer, thereby activating the sequence of processes illustrated in Scheme 2b. Finally step 7 is thermodinamically allowed, and it does not compete with any other step; the value of its rate constant, k_7, which is not relevant for the discussion on quantum yields and efficiencies, is estimated to be around 10^3 s^{-1} (Supporting Information).

We can now discuss the performance of $\mathbf{1}^{6+}$ as a photochemically driven molecular motor when it operates according to the mechanisms illustrated in Scheme 2. The quantum yield of the shuttling process (Φ_{sh}, number of ring shuttling events divided by number of absorbed photons) is given by eq. 3:

$$\Phi_{sh} = \Phi_{et} \times \eta_{rd} \times \eta_{er} \times \eta_{nr} \qquad (3)$$

where Φ_{et} is the quantum yield of the photoinduced electron transfer process that causes the destabilization of the stable conformation A, η_{rd} the efficiency of ring displacement, η_{er} the efficiency of the electronic reset, and η_{nr} the efficiency of the nuclear reset.

The quantum yield of the photoinduced electron transfer process is the same, regardless of the working mechanism, $\Phi_{et} = k_2/(k_2+k_3)$, e. g., 0.16 at 303 K (Scheme 2 and Table 1). The efficiency of the electronic reset, η_{er}, is equal to unity in both mechanisms since back electron transfer takes place in any case (via steps 5 and 6 in the intramolecular mechanism, and via steps 9 and 10 in the **ptz**-assisted one), as shown by lack of any degradation after 10^3 cycles. The efficiency of the nuclear reset, η_{nr}, is equal to 1 in all cases since k_7 does not compete with any other step. Therefore equation 3 reduces to:

$$\Phi_{sh} = \Phi_{et} \times \eta_{rd} \qquad (4)$$

The efficiency η_{rd} depends upon the operating mechanism and the experimental conditions, as shown in Table 3. The values of the quantum yield of ring shuttling, Φ_{sh}, at the various temperatures examined are also gathered in Table 3.

When $\mathbf{1}^{6+}$ works according to the intramolecular mechanism (Scheme 2a), at 303 K $\eta_{rd} = 0.14$ and therefore the quantum yield for the shuttling process, Φ_{sh}, is about 2%. On decreasing temperature, the quantum yield decreases since k_4 (i. e., k_{rd}) refers to a strongly activated process (Figure 5b), whereas ($k_5 + k_4$) (i. e., k_{bet}) is almost temperature independent.

When $\mathbf{1}^{6+}$ works with assistance of **ptz** (Scheme 2b), at 303 K $\eta_{rd} = 0.76$ and $\Phi_{sh} = 12\%$. On decreasing temperature η_{rd} decreases, but Φ_{sh} is still appreciable (4%) at 284 K. On changing the $\mathbf{ptz}^{+}$ concentration, the values of η_{rd} and Φ_{sh} would of course change.

Energetics

The energy available ($\Delta G°_T$) for the shuttling, which could, in principle, be used to do mechanical work, can be estimated on the basis of thermodynamic considerations (see Supporting Information). The energy levels involved in the photoinduced ring shuttling of $\mathbf{1}^{6+}$ at room temperature are shown in Figure 6. Altogether, the fraction F of the excited state energy used for the motion of the ring amounts to ca. 10%, and the overall efficiency of light-to-mechanical energy conversion, $\eta_{en.conv.} = \Phi_{sh} \times F$, is ~1% for the kinetically assisted system and ~0.2% in the case of the intramolecular mechanism (at 303 K). Considering that the nuclear reset (step 7 in Scheme 2a) is around 1 ms, the motor can be driven at a frequency of 10^3 Hz, potentially generating a power of about 3×10^{-17} W per molecule.

CONCLUSIONS

We have shown that in rotaxane $\mathbf{1}^{6+}$ displacement of the ring for approximately 1.3 nm between the two stations $\mathbf{A_1}^{2+}$ and $\mathbf{A_2}^{2+}$, that are placed along the dumbbell-shaped component, can be obtained by light energy inputs without consumption of chemical fuels and formation of waste products. Such photoinduced ring displacement can occur by (i) a purely intramolecular mechanism and (ii) an intermolecular mechanism, involving the assistance of an external electron relay. The system behaves as an autonomous linear motor powered by visible light and its operation takes place in four strokes: destabilization of the stable conformation, displacement of the ring, electronic reset, and nuclear reset.

Each phase (Scheme 2a) corresponds, in kind, to the fuel injection and combustion (A), piston displacement (B), exhaust removal (C), and piston replacement (D) of a four-stroke engine. The timing of the strokes is intrinsic to the molecular motor and cannot be tuned up externally as in fuel-injected car engines. The mechanism relies indeed on the competition between the motion of the ring (step 4) and the back electron transfer (step 5). If the latter process is much faster than the former, the photoinduced electron transfer (step 2) is simply followed by a back electron transfer (step 5), with no relative motion involving the ring. Such a situation would be equivalent to injection of fuel and removal prior to combustion. In the present case, at 303 K, the back electron transfer is 7 times faster than ring displacement, leading to an overall quantum efficiency of the motor of 2%. When the ring shuttling is assisted by the electron relay (Scheme 2b), the "negative" kinetic effect exerted by **ptz** on the back electron transfer increases the overall quantum efficiency of the motor to 12%.

The low efficiency of this motor when it works in an autonomous way with the assistance of an external relay – and even more so when it works purely with an intramolecular mechanism – may seem disappointing, but it should be noted that the fuel (sunlight) is free. Besides being

powered by sunlight and operating as an autonomous motor, the investigated system shows other quite interesting properties: it works in mild environmental conditions, it is remarkably stable and it can be driven at high frequency (kHz). In principle, when working by intramolecular mechanism, it is also suitable for operation at the single-molecule level.

The field of artificial molecular motors is still in its infancy. The construction of an autonomous, sunlight driven molecular motor was a very ambitious task from the outset. Our results show that the structural and functional integration of suitably selected modular units into carefully designed multicomponent molecular systems is indeed a valuable approach.

MATERIALS AND METHODS

The synthesis and the electrochemical and spectroscopic properties of $\mathbf{1}^{6+}$, its dumbbell-shaped component $\mathbf{2}^{6+}$, and the model compound of the photosensitizer unit $\mathbf{3}^{2+}$ (Scheme 1) have been previously reported (37).

Spectroelectrochemical measurements. Spectroelectrochemical measurements in acetonitrile Romil-Hi-Dry were performed in situ with a custom-made OTTLE (optically transparent thin layer electrochemical) cell by using an Agilent Technologies 8543 diode array spectrophotometer. The working and counter electrodes were Pt minigrids (ca. 0.3 cm^2), and the quasi-reference electrode was an Ag wire; all three electrodes are melt-sealed into a polyethylene spacer. The thickness of the layer, determined by spectrophotometry, was about 180 μm.

Photophysical measurements. Measurements were carried out on acetonitrile Merck Uvasol solutions with concentrations ranging from 5.0×10^{-5} to 1.0×10^{-4} mol L^{-1}. UV-Vis absorption spectra were recorded at room temperature on air equilibrated solutions with a Perkin Elmer λ40 spectrophotometer. Luminescence spectra were obtained with a Perkin Elmer LS-50

spectrofluorimeter, equipped with a Hamamatsu R928 phototube, on solutions degassed with four freeze-pump-thaw cycles and sealed under vacuum (7×10^{-9} bar). The experimental error on the wavelength values is estimated to be ±1 nm.

Flash photolysis experiments. Luminescence decay and transient absorption experiments were performed in acetonitrile Merck Uvasol by exciting the sample with 10 ns (fwmh) pulses of a Continuum Surelite I-10 Nd:YAG laser. In the transient absorption studies, a 150 W Xe lamp (Applied Photophysics model 720; power supply, model 620) perpendicular to the laser beam was used as a probing light; for the kinetic investigations in the 0–10 μs time window, a pulsing unit (Applied Photophysics model 03-102, 2 ms pulses) was also employed. Excitation was performed at λ=532 nm, obtained by frequency doubling. A shutter was placed between the lamp and the sample, and opened only during the measurements to prevent phototube fatigue and photodecomposition. Suitable pre- and post-cutoff and bandpass filters were also used to avoid photodecomposition and interferences from scattered light. The light was collected in a PTI monochromator (model 01-001; 1200 lines/mm grating; slit width, 0.25 mm; resolution, 1 nm), detected by a Hamamatsu R928 tube, and recorded on a Tektronix TDS380 (400 MHz) digital oscilloscope connected to a PC. Synchronous timing of the system was achieved by means of a built-in-house digital logic circuit. The absorption transient decays were plotted as $\Delta A = \log(I_0/I_t)$ versus time, where I_0 and I_t were the probing light intensity prior to the laser pulse and after delay t, respectively. Each decay was obtained by averaging at least 20 pulses. Transient absorption spectra were obtained from the decays measured at various wavelengths (5 nm increment), by sampling the absorbance changes at constant delay time. In the determination of the shift of λ_{max}, a wavelength increment of 1 nm in the 350-440 nm region was adopted; to obtain a significant comparison between the bands of the rotaxane and of its dumbbell-shaped component, the decay at each wavelength was measured in parallel for otherwise identical

solutions of $\mathbf{1}^{6+}$ and $\mathbf{2}^{6+}$. The same laser/monochromator/phototube setup was employed to measure luminescence lifetimes.

The accuracy on the wavelength values was estimated to be ±2 nm. The experimental error was 4% for the lifetime values and 20% for the quantum yield of the photoinduced electron transfer processes.

ACKNOWLEDGMENTS

The authors wish to thank Dr. Lucia Flamigni for useful discussion. This research was supported by the Ministry of Education, University and Research in Italy, and by the National Science Foundation in the United States. The European Union is gratefully acknowledged for support under the auspices of the Molecular-Level Devices and Machines Network, the Biomach project and a Marie Curie Individual Fellowship to B.F.

REFERENCES

1. Balzani, V., Credi, A., Raymo, F. M. & Stoddart, J. F. (2000) *Angew. Chem. Int. Ed.* **39**, 3348–3391.
2. Stoddart, J. F. ed. (2001) *Acc. Chem. Res.* **34(6)**, Special issue on Molecular Machines.
3. Sauvage, J.-P. ed. (2001) *Struct. Bond.* **99**, Special volume on Molecular Machines and Motors.
4. Balzani, V., Credi, A. & Venturi, M. (2003) *Molecular Devices and Machines – A Journey into the Nano World* (Wiley-VCH, Weinheim).
5. Kelly, T. R. ed. (2005) *Top. Curr. Chem.* **262**, Special volume on Molecular Motors.
6. Schliwa, M. ed. (2002) *Molecular Motors* (Wiley-VCH, Weinheim).

7. Oster, G. & Wang, H. (2003) *Trends Cell Biol.* **13**, 114–121.
8. Goodsell, D. S. (2004) *Bionanotechnology: Lessons from Nature* (Wiley, New York).
9. Jones, R. A. L. (2005) *Soft Machines - Nanotechnology and Life* (Oxford University Press, Oxford)
10. Gomez-Lopez, M., Prece, J. A. & Stoddart, J. F. (1996) *Nanotechnology* **7**, 183–192.
11. Lehn, J.-M. (2002) *Proc. Natl. Acad. Sci. USA* **99**, 4763–4768.
12. Murakami, H., Kawabuchi, A., Kotoo, K., Kunitake, M. & Nakashima, N. (1997) *J. Am. Chem. Soc.* **119**, 7605–7606.
13. Steinberg-Yfrach, G., Rigaud, J.-L., Durantini, E. N., Moore, A. L., Gust, D. & Moore, T. A. (1998) *Nature* **392**, 479–482.
14. Kelly, T. R., De Silva, H. & Silva, R.A. (1999) *Nature* **401**, 150–152.
15. Koumura, N., Zijlstra, R. W., van Delden, R. A., Harada, N. & Feringa, B.L. (1999) *Nature* **401**, 152–155.
16. Brouwer, A. M. Frochot, C., Gatti, F. G., Leigh, D. A., Mottier, L., Paolucci, F., Roffia, S. & Wurpel G. W. H. (2001) *Science* **291**, 2124–2128.
17. Stanier, C. A., Alderman, S. J., Claridge, T. D. W. & Anderson, H. L. (2002) *Angew. Chem. Int. Ed.* **41**, 1769–1772.
18. Leigh, D. A., Wong, J. K. Y., Dehez, F. & Zerbetto, F. (2003) *Nature* **424**, 174–179.
19. Badjic, J. D., Balzani, V., Credi, A., Silvi, S. & Stoddart, J. F. (2004) *Science* **303**, 1845–1849.
20. Hernandez, J. V., Kay, E. R. & Leigh, D. A. (2004) *Science* **306**, 1532–1537.
21. Mobian, P., Kern, J.-M. & Sauvage, J.-P. (2004) *Angew. Chem. Int. Ed.* **43**, 2392–2395.
22. Abraham, W., Grubert, L., Grummt, U. W. & Buck, K. (2004) *Chem. Eur. J.* **10**, 3562–3568.
23. Shin, J.-S. & Pierce, N. H. (2004) *J. Am. Chem. Soc.* **126**, 10834–10835.
24. Wang, Q.C., Qu, D.H., Ren, J., Chen, K. C. & Tian H. (2004) *Angew. Chem. Int. Ed.* **43**, 2661–2665.
25. Sherman, W. B. & Seeman, N. C. (2004) *Nano Lett.* **4**, 1203–1207.
26. Astumian, R. D. (2005) *Proc. Natl. Acad. Sci. USA*, **102**, 1843–1847.
27. Flood, A. H., Peters, A. J., Vignon, S. A., Steuerman, D. W., Tseng, H.-R., Kang, S., Heath, J. R. & Stoddart, J. F. (2004) *Chem. Eur. J.* **10**, 6558–6564.

28. Zheng X. L. Mulcahy, M. E., Horinek, D., Galeotti, F., Magnera, T. F. & Michl J. (2004) *J. Am. Chem. Soc.* **126**, 4540–4542.
29. Katz, E., Lioubashevsky, O. & Willner, I. (2004) *J. Am. Chem. Soc.* **126**, 15520–15532.
30. Kocer A., Walko, M., Meijberg, W. & Feringa, B. L. (2005) *Science* **309**, 755–758.
31. Liu, Y., Flood, A. H., Bonvallet, P. A., Vignon, S. A., Northrop, B. H., Tseng, H.-R., Jeppesen, J. O., Huang, T. J., Brough, B., Baller, M., Magonov, S., Solares, S. D., Goddard, W. A., Ho, C.-M. & Stoddart, J. F. (2005) *J. Am. Chem. Soc.* **127**, 9745–9759.
32. Nguyen, T. D., Tseng, H.-R., Celestre, P. C., Flood, A. H., Liu, Y., Stoddart, J. F. & Zink, J. I. (2005) *Proc. Natl. Acad. Sci. USA* **102**, 10029–10034.
33. Berná, J., Leigh, D. A., Lubomska, M., Mendoza, S. M., Pérez, E. M., Rudolf, P., Teobaldi, G. & Zerbetto, F. (2005) *Nature Mater.* **4**, 704–710.
34. Tian, Y. & Mao, C. D. (2004) *J. Am. Chem. Soc.* **126**, 11410–11411.
35. Tian, Y., He, Y., Chen, Y., Yin, P. & Mao, C. D. (2005) *Angew. Chem. Int. Ed.* **44**, 4355–4358.
36. Bath, J., Green, S. J. & Turberfield, A. J. (2005) *Angew. Chem. Int. Ed.* **44**, 4358–4361.
37. Ashton, P. R., Ballardini, R., Balzani, V., Credi, A., Dress, K. R., Ishow, E., Kleverlaan, C. J., Kocian, O., Preece, J. A., Spencer, N., J Stoddart, J. F., Venturi, M. & Wenger, S. (2000) *Chem. Eur. J.* **6**, 3558–3574.
38. Watanabe, T. & Honda, K. (1982) *J. Phys. Chem.* **86**, 2617–2619.
39. McAskill, N. A. (1984) *Aust. J. Chem.* **37**, 1579–1592.
40. Kowert, B. A., Marcoux, L. & Bard, A. J. (1972) *J. Am. Chem. Soc.* **94**, 5538–5550.
41. Hanson, P. & Norman, R. O. C. (1973) *J. Chem. Soc., Perkin Trans. 2*, 264–271.
42. Tseng, H.-R. Vignon, S. A., Celestre, P. C., Perkins, J., Jeppesen, J. O., Di Fabio, A., Ballardini, R., Gandolfi, M. T., Venturi, M., Balzani, V. & Stoddart, J. F. (2004) *Chem. Eur. J.* **10**, 155–172.

CAPTIONS TO SCHEMES AND FIGURES

Scheme 1. Structural formulas of rotaxane $\mathbf{1}^{6+}$, its dumbbell-shaped component $\mathbf{2}^{6+}$, and model compound $\mathbf{3}^{2+}$.

Scheme 2. Mechanisms of the photochemically driven ring shuttling in $\mathbf{1}^{6+}$. **a**, intramolecular mechanism. **b**, shuttling assisted by an electron relay. **c**, graphical representation of how the energy profile of shuttling changes upon reduction of $\mathbf{A_1}^{2+}$ and the location of the ring at $\mathbf{A_1}^{2+}$ (blue) or $\mathbf{A_2}^{2+}$ (magenta) for each molecular structure illustrated.

Figure 1. UV-Visible difference absorption spectra obtained upon electrochemical reduction of $\mathbf{1}^{6+}$ (——) and $\mathbf{2}^{6+}$ (– – –) at –0.50 V versus SCE in a spectroelectrochemical thin layer cell (5.0×10^{-4} mol L^{-1} acetonitrile solution, room temperature). The spectra were normalized to the intense band peaking at 392 nm for $\mathbf{1}^{6+}$. Inset shows the detail of the spectra in the 370-405 nm region.

Figure 2. Transient absorption kinetics, monitored at λ_{iso} = 398 nm, of rotaxane $\mathbf{1}^{6+}$, dumbbell-shaped component $\mathbf{2}^{6+}$, and model compound $\mathbf{3}^{2+}$ after 532-nm nanosecond laser excitation (degassed acetonitrile solution, room temperature).

Figure 3. Transient UV-Vis absorption difference spectra of a deaerated acetonitrile solution containing 1.0×10^{-4} mol L^{-4} $\mathbf{1}^{6+}$ and 5.0×10^{-5} mol L^{-1} **ptz**, recorded 50 μs after 532-nm laser excitation at room temperature. Inset shows the normalized transient absorption decays monitored at 520 (——) and 600 (· · · ·) nm, which correspond to signals assigned to $\mathbf{ptz}^{+}$ and $\mathbf{A_1}^{+}$, respectively.

Figure 4. a, Time dependence of the wavelength of the absorption maximum (λ_{max}) of the UV band of photogenerated $\mathbf{A_1}^+$ for $\mathbf{1}^{6+}$ (full circles) and $\mathbf{2}^{6+}$ (empty circles) at 303 K. The full line represents the monoexponential data fit used to obtain k_{rd} for $\mathbf{1}^{6+}$. **b**, Diagram showing the temperature dependence of k_{rd}.

Figure 5. Energy level diagram for the processes taking place in rotaxane $\mathbf{1}^{6+}$ when it works as a light driven molecular motor based on intramolecular processes at room temperature (see Scheme 2a). The energy of a 532-nm photon (225 kJ mol^{-1}) is employed to produce the long-lived excited state of the $\mathbf{P}^{2+}$ component (205 kJ mol^{-1}, E), which decays by electron transfer to the $\mathbf{A_1}^{2+}$ station (B) with ca. 14% yield. An energy of 10 kJ mol^{-1} is then released in the Brownian motion of the ring **R** over the 50 kJ mol^{-1} barrier (forward stroke) from $\mathbf{A_1}^+$ to $\mathbf{A_2}^{2+}$ (C). A further 145 kJ mol^{-1} is used to transfer the electron from $\mathbf{A_1}^+$ back to $\mathbf{P}^{3+}$ (D) and the remaining 8 kJ mol^{-1} is released in the motion of the ring (backward stroke) from $\mathbf{A_2}^{2+}$ to $\mathbf{A_1}^{2+}$ (A).

Table 1. Luminescence data and related parameters in deaerated acetonitrile solution.

		T (K)				
		284	288	293	299	303
τ_0 (ns)	$\mathbf{3}^{2+}$	1030	990	900	820	770
τ (ns)	$\mathbf{1}^{6+}$	890	850	780	710	650
	$\mathbf{2}^{6+}$	870	830	760	680	620
k_{et} (s^{-1})	$\mathbf{1}^{6+}$	1.5×10^5	1.7×10^5	1.7×10^5	1.9×10^5	2.5×10^5
	$\mathbf{2}^{6+}$	1.8×10^5	2.0×10^5	2.1×10^5	2.4×10^5	3.1×10^5
Φ_{et}	$\mathbf{1}^{6+}$	0.14	0.14	0.14	0.13	0.16
	$\mathbf{2}^{6+}$	0.15	0.16	0.16	0.17	0.19

Table 2. Kinetic data for photoinduced processes of $\mathbf{1}^{6+}$ in deaerated acetonitrile solution in the temperature range 284-303 K. The corresponding data for $\mathbf{2}^{6+}$ are reported in parentheses.

	T (K)				
	284	288	293	299	303
k_{et} (s^{-1})	1.5×10^5 (1.8×10^5)	1.7×10^5 (2.0×10^5)	1.7×10^5 (2.1×10^5)	1.8×10^5 (2.4×10^5)	2.5×10^5 (3.1×10^5)
k_{bet} (s^{-1})	1.4×10^5 (5.4×10^5)	1.4×10^5 (5.9×10^5)	1.4×10^5 (6.7×10^5)	1.4×10^5 (7.0×10^5)	1.5×10^5 (6.9×10^5)
k_{ptz} (L mol^{-1} s^{-1})	7.9×10^8 (5.0×10^8)	8.4×10^8 (5.0×10^8)	7.6×10^8 (4.9×10^8)	7.8×10^8 (4.8×10^8)	8.1×10^8 (4.8×10^8)
k_{rd} (s^{-1})	8.1×10^2	1.8×10^3	3.5×10^3	1.3×10^4	2.1×10^4
τ_{bet} (μs)	7.4 (1.8)	7.1 (1.7)	7.0 (1.5)	7.1 (1.4)	6.7 (1.4)
τ_{rd} (μs)	1230	550	285	78	47

Subscript legend: et, photoinduced electron transfer (Scheme 2a, step 2); bet, back electron transfer (Scheme 2a, steps 5 and 6); ptz, bimolecular electron transfer between the $\mathbf{A_1}^+$ unit and $\mathbf{ptz}^+$ (Scheme 2b, steps 9 and 10); rd, displacement of the ring from $\mathbf{A_1}^+$ to the $\mathbf{A_2}^{2+}$ station corresponding to the shift of the transient absorption maximum of the $\mathbf{A_1}^+$ unit, (Scheme 2, a and b, step 4).

Table 3. Values of the efficiency of ring displacement, η_{rd}, and quantum yield of ring shuttling, Φ_{sh}, for $\mathbf{1}^{6+}$ in the temperature range 284-303 K. Conditions: deaerated acetonitrile solution, and for the assisted mechanism of Scheme 2b, [**ptz**]=5.0×10^{-5} mol L^{-1} (for more details see Supporting Information).

		T (K)				
		284	288	293	299	303
	k_4 (s^{-1})	8.1×10^2	1.8×10^3	3.5×10^3	1.3×10^4	2.1×10^4
Intramolecular mechanism (Scheme 2a)	k_5 (s^{-1})	1.4×10^5	1.4×10^5	1.4×10^5	1.3×10^5	1.3×10^5
	η_{rd}	<0.01	0.01	0.025	0.09	0.14
	Φ_{sh}	<0.001	0.002	0.004	0.015	0.02
Mechanism with assistance of phenothiazine (Scheme 2b)	$k_9[\mathbf{ptz}^+]_0$ (s^{-1})	2.5×10^3	3.2×10^3	3.3×10^3	5.1×10^3	6.7×10^3
	η_{rd}	0.25	0.36	0.51	0.72	0.76
	Φ_{sh}	0.04	0.06	0.08	0.12	0.12

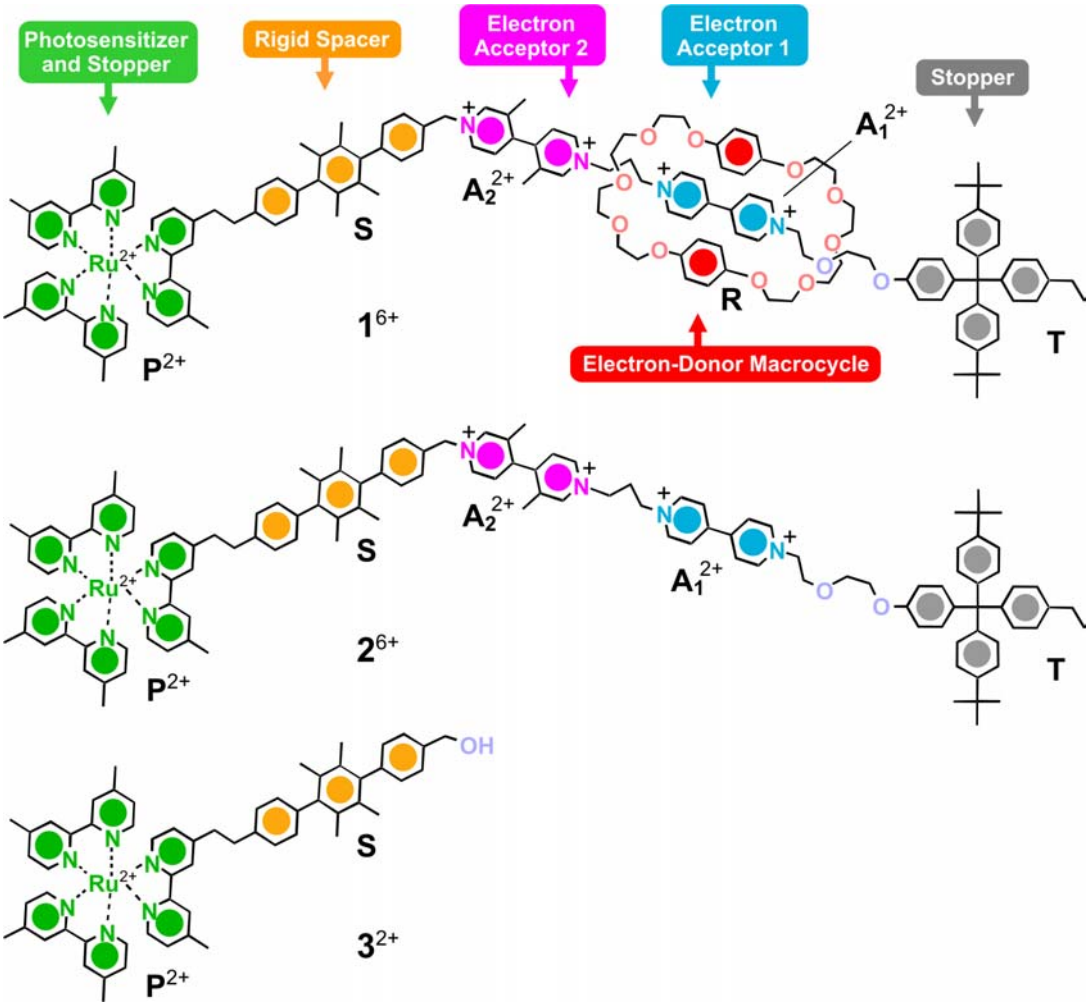
Photosensitizer and Stopper
Rigid Spacer
Electron Acceptor 2
Electron Acceptor 1
Stopper
A_1^{2+}
A_2^{2+}
S
R
T
1^{6+}
P^{2+}
Electron-Donor Macrocycle
2^{6+}
OH
3^{2+}

Scheme 1

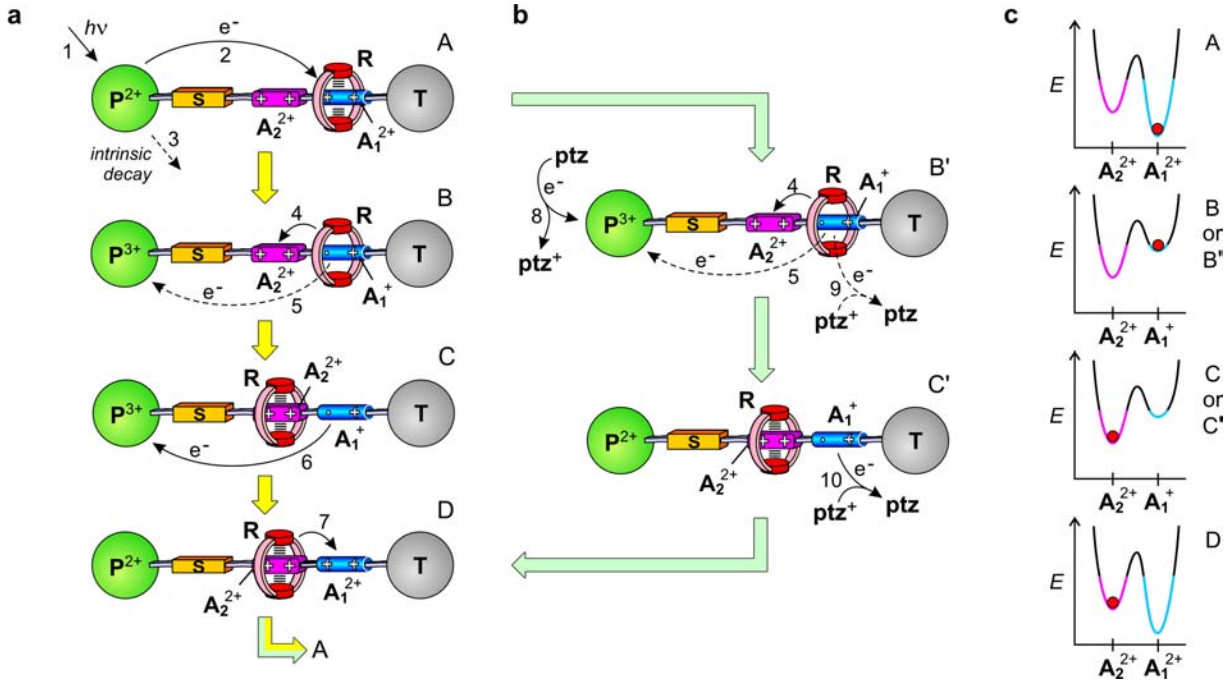
a
b
c
hν
1
e⁻
2
intrinsic
decay
3
A
B
C
D
R
S
T
P²⁺
P³⁺
A₂²⁺
A₁²⁺
A₁⁺
4
5
6
7
A
ptz
e⁻
8
ptz⁺
B'
9
ptz
C'
10
E
A
B
or
B'
C
or
C'
D

Scheme 2

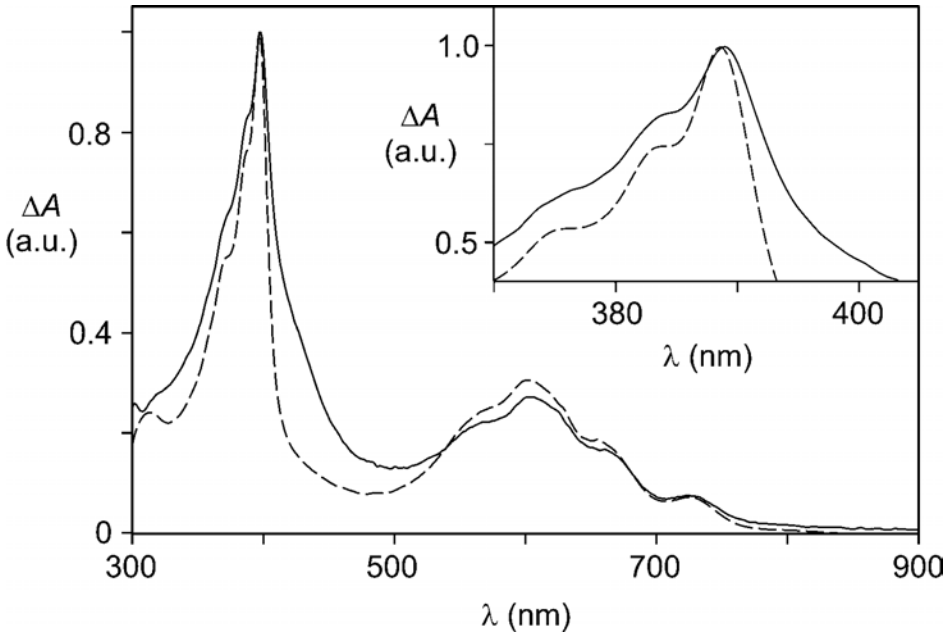

Figure 1

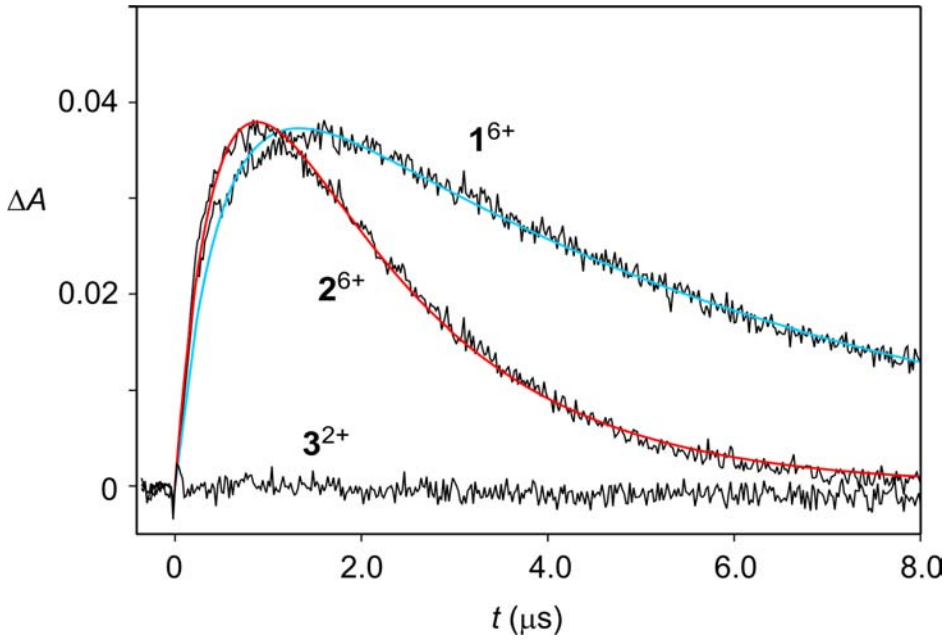

Figure 2

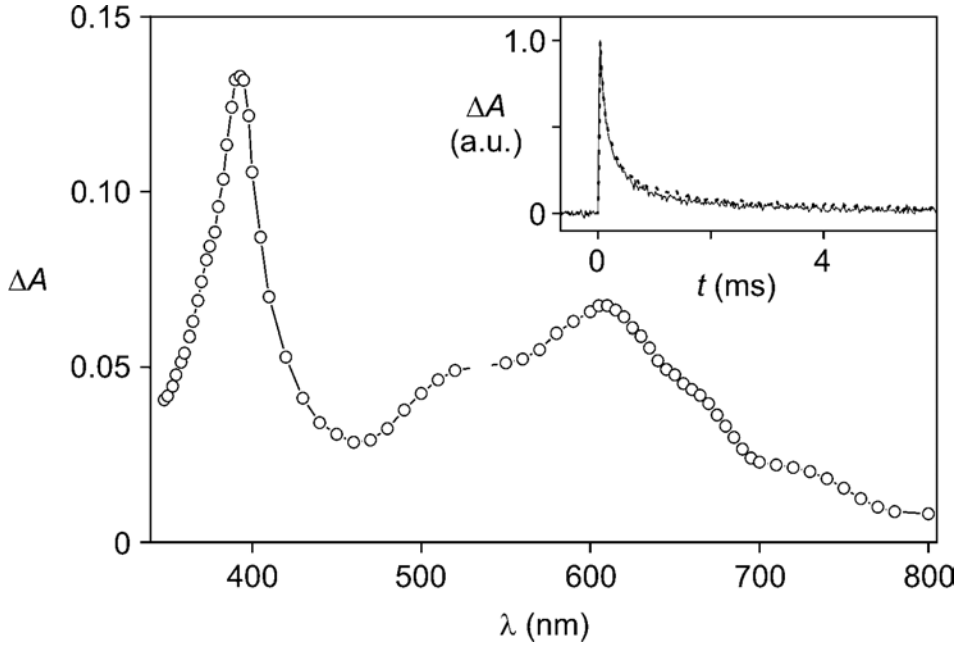

Figure 3

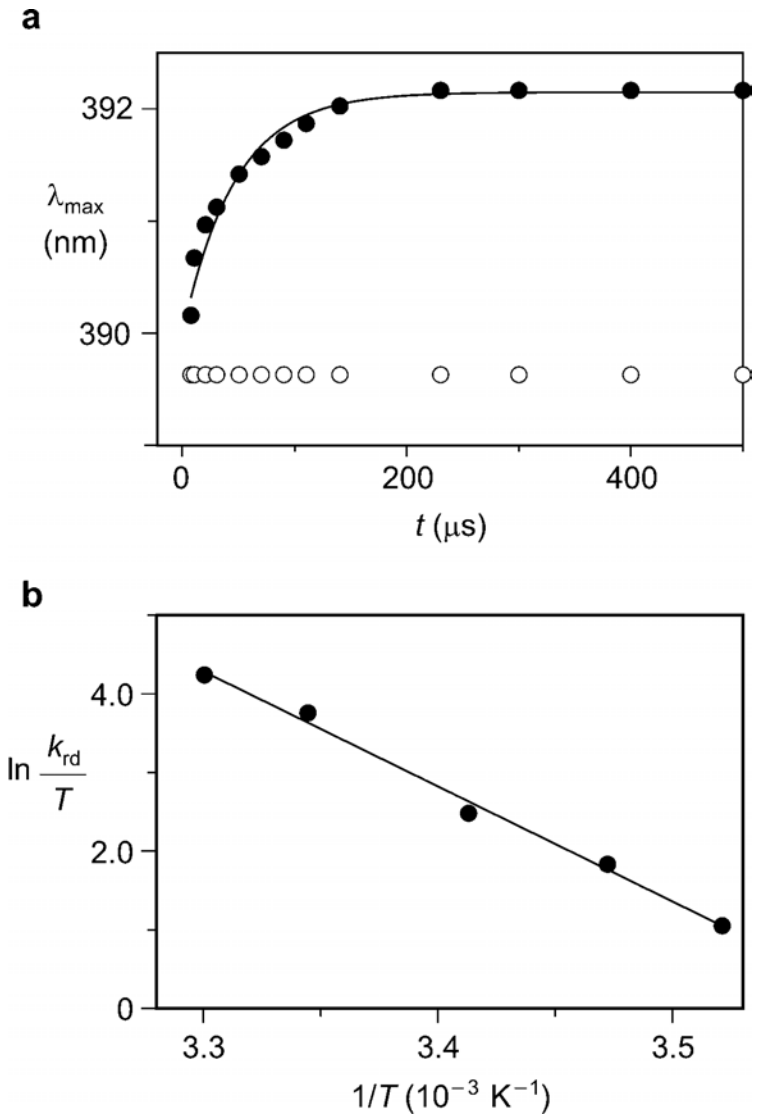

Figure 4

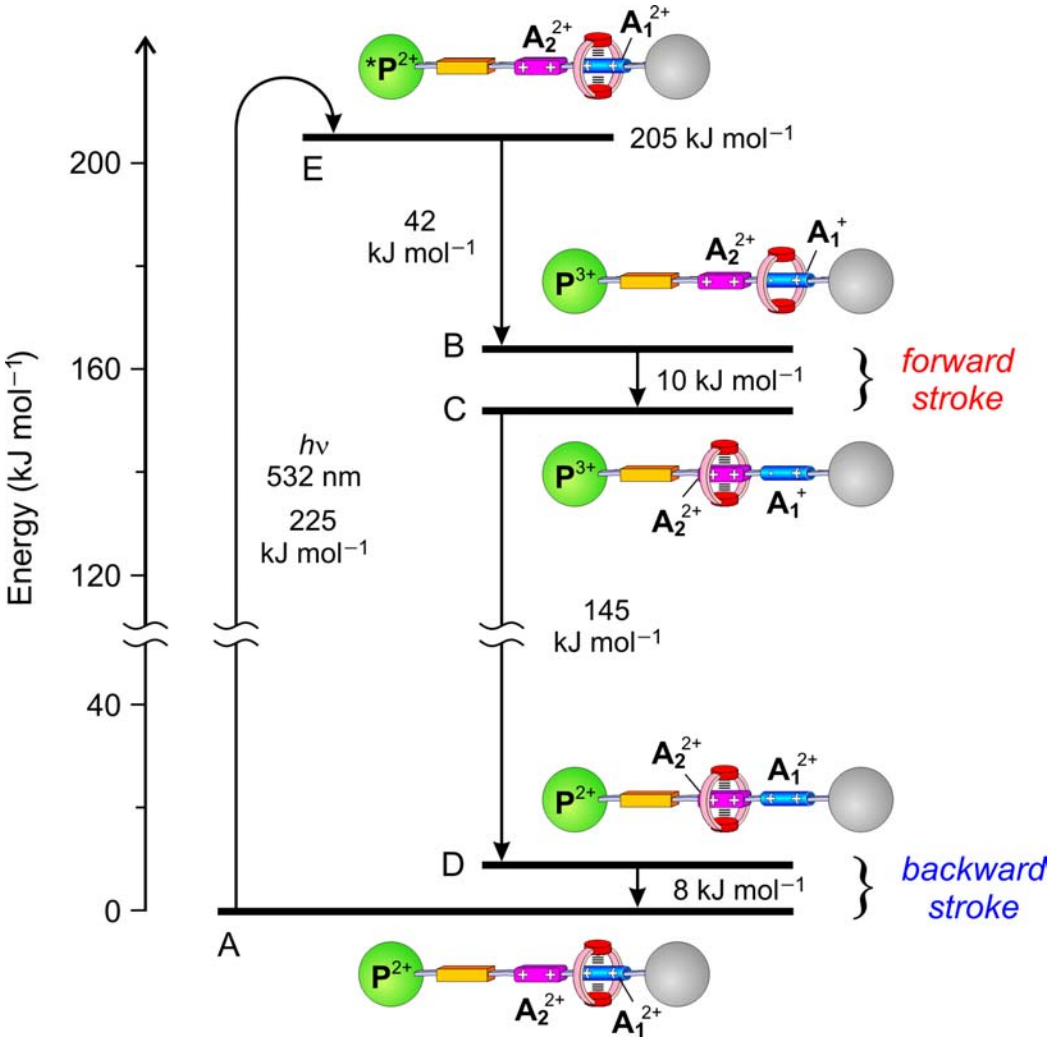
Energy (kJ mol⁻¹)
200
160
120
40
0
*P2+
A2 2+
A1 2+
205 kJ mol⁻¹
E
42
kJ mol⁻¹
P3+
A2 2+
A1 +
B
10 kJ mol⁻¹
forward
stroke
C
hν
532 nm
225
kJ mol⁻¹
P3+
A2 2+
A1 +
145
kJ mol⁻¹
P2+
A2 2+
A1 2+
D
8 kJ mol⁻¹
backward
stroke
A
P2+
A2 2+
A1 2+

Figure 5